Modeling of High-Concentrator Photovoltaic Systems for Utility-Scale Applications

Yong Sin Kim

Abstract The levelized cost of energy (LCOE) is widely used for evaluating the cost of energy generation across technologies. In a utility-scale high-concentrator photovoltaic system (HCPV), capacity factor (CF) and ground-coverage ratio (GCR) are the two fundamental drivers for determining the LCOE. However the LCOE is a complex function of various parameters, which is not explicitly defined in terms of these two factors. In this chapter, based on a cost function that simplifies the LCOE in terms of CF and GCR, the method for modeling utility-scale HCPV systems is considered.

1 Introduction

As the price of fossil fuel and environmental concern increases, so does the demand for renewable energy. Although numerous utility-scale photovoltaic (PV) systems have been researched and installed during the last several decades, the cost of energy generation has remained high compared with other types of energy-generation systems. In comparing the energy generation cost for utility-scale power plants, levelized cost of energy (LCOE) is widely used and defined as the cost of generating electricity over the system's lifetime accounting for initial investment, financing, cost for operations and maintenance, cost of fuel, and some other expenses [1, 2]. One of the essential way to reduce the LCOE of a utility-scale PV system is to optimize system-specific parameters through accurate system modeling.

There are two fundamental drivers for the LCOE of utility-scale PV systems: capacity factor (CF) and system ground-coverage ratio (GCR) [3–5]. CF represents the total amount of energy that the plant produces during a certain period of time divided by the total amount of energy that the plant would have produced at its full capacity, which depends on the locations of the site, PV and inverter efficiency, and

Y.S. Kim (✉)
School of Electrical Engineering, Korea University, Seoul, South Korea
e-mail: shonkim@korea.ac.kr

P. Pérez-Higueras and E.F. Fernández (eds.), *High Concentrator Photovoltaics*,
Green Energy and Technology, DOI 10.1007/978-3-319-15039-0_6

tracking method. GCR is defined as the ratio of total PV area to the total land used. The highest CFs are generated with dual-axis trackers that follow the sun throughout the day and keep the PV module oriented toward the sun for maximizing energy generation. The longer the time spent tracking the sun (indicating the higher CF), however, the more space between trackers is needed to minimize the self-shading effect [3–6]. As a result, GCR is reduced and LCOE increases due to additional overhead in terms of land requirements, site preparation and maintenance, electrical wiring, and trenching.

For accurately modeling utility-scale high-concentrator PV (HCPV) systems, conventional modeling based on flat panels is inadequate. Various tracking methods based on flat panels have been investigated in [4], in which energy yield—defined as the ratio of total energy generated to the peak energy—and GCR are mostly considered. However, unlike CF, energy yield does not consider time dependency and thus is not suitable because the insolation changes throughout the day. Furthermore, lack of an electrical model for power optimization lowers the accuracy in modeling the total power harvested under shading conditions.

HCPV systems with narrow acceptance angles requires accurate dual-axis tracking resulting in the trade-off between tracker array spacing, self-shading loss, and land use. When simulating utility-scale HCPV systems after modeling, the computational time for finding the optimum configuration for given system parameters increases exponentially as the number of trackers increases. In this chapter, system modeling, as well as the method by which to reduce computational time in simulating utility-scale HCPV Systems, will be covered.

2 Cost Function

Modeling starts from defining two-tracker space-related parameters, i.e., GCR and CF as

$$\mathrm{GCR} = \sum A_{\mathrm{module}} \Big/ A_{\mathrm{land}} \tag{1}$$

$$\mathrm{CF} = \int_{t_1}^{t_2} P(t)\mathrm{d}t / [(t_2 - t_1)P_{\max}] \tag{2}$$

where A_{module} is the area of a CPV module; A_{land} is the total land area for the system; $P(t)$ is the output power generated by the system at a given time t; and $P_{\max}$ is the maximum power available by the system. Then LCOE can be simplified as

$$\mathrm{LCOE} = \frac{\sum C}{\int_{t_1}^{t_2} P(t)\mathrm{d}t} = \frac{C_{\mathrm{others}} + C_{\mathrm{land}}A_{\mathrm{land}}}{\mathrm{CF}(t_2 - t_1)P_{\max}} \tag{3}$$

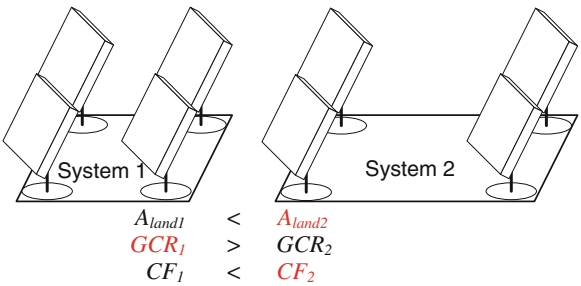

Fig. 1 Capacity factor (*CF*) versus ground coverage ratio (*GCR*) in CPV systems

where the sum of C is the cost over the system's lifetime, C_{land} is the cost of a unit land; and C_{others} is overall cost not related to land. With a system constant k, LCOE can be expressed as

$$\text{LCOE} = \frac{1 + C_{\text{land}} A_{\text{land}} / C_{\text{others}}}{\text{CF}(t_2 - t_1) P_{\max} / C_{\text{others}}} = \frac{1 + \frac{k}{\text{GCR}}}{\text{CF}(t_2 - t_1) P_{\max} / C_{\text{others}}} \tag{4}$$

Thus, the cost function F can be expressed by the relationship between CF and GCR with k as [7]:

$$F = \frac{1 + \frac{k}{\text{GCR}}}{\text{CF}} \propto \text{LCOE} \tag{5}$$

If F is minimized, so is LCOE because F is linearly proportional to LCOE. Previous analysis using complicated equations to calculate and minimize LCOE is now reduced to a simple equation that has one system parameter and two variables. Figure 1 shows trackers in two different systems. The total area of the system 1 is smaller than that of the system 2, resulting in higher GCR but less CF due to larger self-shading loss; this will be covered later in this chapter.

3 Solar Radiation

To estimate total power harvested from a system, it is crucial to have accurate solar radiation data at the site where the system is deployed. In this section, we describe the Sun's position, air mass (AM), and weather function to obtain direct normal irradiance (DNI) data on an hourly basis.

3.1 The Sun's Position

The Sun's apparent position varies with the location of observer and the time, which can be described by two angles: the elevation angle α and the azimuth angle

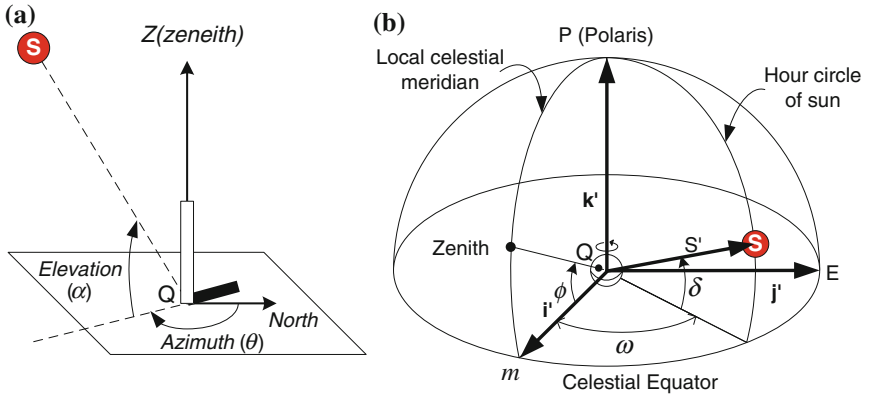

Fig. 2 **a** Earth surface coordinate system for an observer at location Q. **b** Earth center coordinate system with hour angel ω, declination δ, and latitude ϕ at location Q

θ as shown in Fig. 2a. The α is the angular height of the geometric center of the Sun from the horizon, and the θ is the clockwise angle on the horizontal plane from the north-pointing coordinate axis to the projection of the Sun's central ray. α and θ at location Q can be expressed in terms of the latitude ϕ, the declination of the Sun δ, and the hour angle ω in Fig. 2b as [8]:

$$\begin{aligned} \sin\alpha &= \cos\phi\cos\delta\cos\omega + \sin\phi\sin\delta \\ \cos\alpha\sin\theta &= \cos\delta\sin\omega \\ \cos\alpha\cos\theta &= -\sin\phi\cos\delta\cos\omega + \cos\phi\sin\delta \end{aligned} \tag{6}$$

3.2 Air Mass and Weather Function

Extraterrestrial radiation I_E, solar radiation incident outside of the earth's atmosphere, varies by ±3 % throughout a year depending on the Earth–Sun distance. It can be expressed as

$$I_E(n) = I_0 \cdot \left(\frac{\overline{R_{ES}}}{R_{ES}}\right)^2 \approx I_0\left[1 + 0.033\cos\left(\frac{360\cdot n}{365}\right)\right] \tag{7}$$

where $I_0 = 1367$ W/m^2 is the solar constant; R_{ES} is the actual earth-sun distance; $\overline{R_{ES}}$ is the average value of R_{ES}; and n is the nth day in a year [9]. Solar radiation, which is defined as solar energy received on the Earth's surface, is the sum of DNI and diffused radiation after scattering in the atmosphere. As the rays travel through the

atmosphere longer, solar radiation attenuates more due to increased probability of scattering and absorption. Solar radiation discussed in [4] neglects this attenuation.

AM describes the attenuation of solar radiation and is defined as the optical path length of solar radiation through the earth's atmosphere. AM incorporates the curvature of the earth as a function of α and can be expressed as [10]:

$$\mathrm{AM}(\alpha) = \frac{1}{\sin\alpha + 0.50572 \cdot (6.07995 + \alpha)^{-1.6364}} \tag{8}$$

Denoting I_{D} as the intensity of solar radiation reaching the earth's surface at normal incident, approximately 70 % of the radiation incident on the atmosphere is transmitted to the Earth's surface as [11]:

$$I_{\mathrm{D}}(n,\alpha) = I_{\mathrm{E}}(n) \cdot 0.7^{\mathrm{AM}(\alpha)^{0.678}} \tag{9}$$

However, sunlight intensity depends not only on the day of a year and the Sun's elevation but also on the site location as shown in Fig. 3. The α is a function of time. Thus, the intensity of direct normal incident of sunlight on an hourly basis needs to include the weather function $W(n)$ of the site as

$$I_{\mathrm{D}}(n,\alpha) = I_{\mathrm{E}}(n) \cdot W(n) \cdot 0.7^{\mathrm{AM}(\alpha)^{0.678}} \tag{10}$$

The monthly average DNI values from various sources, such as NASA and NREL (both TMY2 and TMY3 are available), as shown in Fig. 4, can be used for obtaining $W(n)$, which can be expressed as

$$\overline{I_{\mathrm{D}}(m)} = \frac{1}{n_{\mathrm{E}} - n_{\mathrm{S}}} \frac{2}{\alpha_{\max}} \int_{n_{\mathrm{S}}}^{n_{\mathrm{E}}} \int_{0}^{\alpha_{\max}} I_{\mathrm{E}}(n) \cdot W(n) \cdot 0.7^{\mathrm{AM}(\alpha)^{0.678}} \mathrm{d}\alpha \mathrm{d}n \tag{11}$$

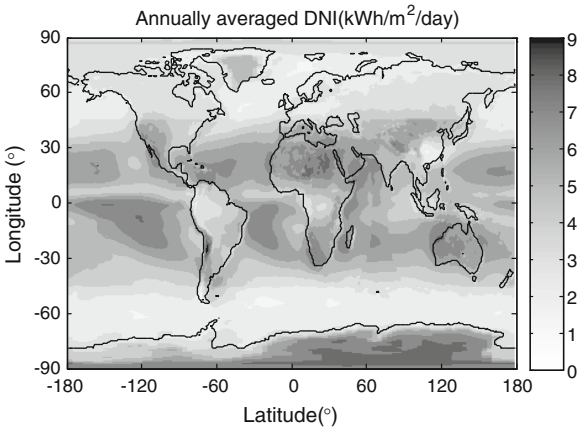

Fig. 3 Annually averaged DNI of the world

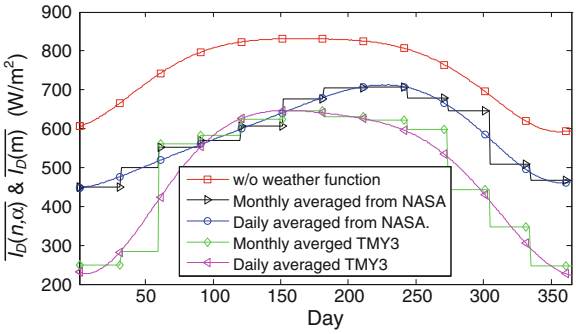

Fig. 4 Monthly and daily averaged direct normal incident radiation in a year for a location at latitude of 37° and longitude −120°

where m is the month of a year; and n_E and n_S are the end and the start days of the month, respectively. α_{max} represents the maximum α on the nth day. For the location at latitude of 37° and longitude −120°, for example, the fifth-order polynomial curve fit in the least-squares sense to the monthly averaged DNI from NASA gives

$$W(n) = 1.09 \times 10^{-12} n^5 - 9.10 \times 10^{-10} n^4 + 2.20 \times 10^{-7} n^3 \cdots - 1.04 \times 10^{-5} n^2 - 6.89 \times 10^{-4} n + 0.74 \tag{12}$$

Figure 4 also compares DNI values produce by Eqs. (9) and (10). The hourly DNI at the given location is depicted in Fig. 5. We will consider this hourly DNI data throughout the simulations.

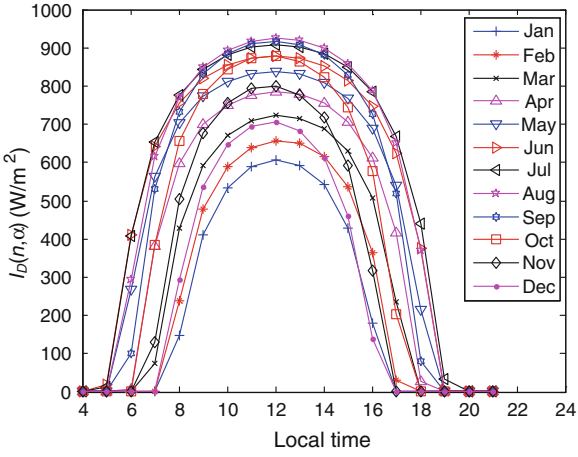

Fig. 5 Hourly direct normal incident radiation at latitude 37° and longitude −120° for the first day of each month

4 Self-shading by Dual-Axis Trackers

As discussed previously, HCPV systems with dual-axis trackers can maximize CF by tracking the Sun throughout a day. Especially in the morning and the evening, however, this tracker array poses a self-shading problem, which in turn causes power loss and thus reduces CF. To alleviate the self-shading problem, the optimal spacing between trackers should be determined [5, 7]. Figure 6 depicts a dual-axis tracker whose modules are normal to the sunlight in X–Z plane.

To obtain shaded area on the ground, we need to know the $L_0(t)$, and $L_S(t)$ at time t can be given by:

$$L_0(t) = \frac{H(t) - P}{\tan(\alpha(t))} = \frac{h/2/\cos(\alpha(t)) - P}{\tan(\alpha(t))} \tag{13}$$

$$L_S(t) = L(t) - L_0(t) = \frac{h}{\sin(\alpha(t))} - \frac{h/2/\cos(\alpha(t)) - P}{\tan(\alpha(t))} \tag{14}$$

where h is the height of the module array; P is the height of a pole; $H(t)$ is the hypotenuse of the right-angled triangle with one side formed by the half-height of the module array; and $\alpha(t)$ is the α at time t. Then, four vertices—$V_{LB}(t)$, $V_{LT}(t)$, $V_{RB}(t)$, and $V_{RT}(t)$—of the shaded area for the tracker located at (0, 0) can be obtained as

$$\begin{aligned}
V_{LB}(t) &= (-L_0(t)\cos\phi(t) - w/2 \cdot \sin\phi(t), L_0(t)\sin\phi(t) - w/2 \cdot \cos\phi(t)) \\
V_{LT}(t) &= (-L_S(t)\cos\phi(t) - w/2 \cdot \sin\phi(t), L_S(t)\sin\phi(t) - w/2 \cdot \cos\phi(t)) \\
V_{RB}(t) &= (-L_0(t)\cos\phi(t) + w/2 \cdot \sin\phi(t), L_0(t)\sin\phi(t) + w/2 \cdot \cos\phi(t)) \\
V_{RT}(t) &= (-L_S(t)\cos\phi(t) + w/2 \cdot \sin\phi(t), L_S(t)\sin\phi(t) + w/2 \cdot \cos\phi(t))
\end{aligned} \tag{15}$$

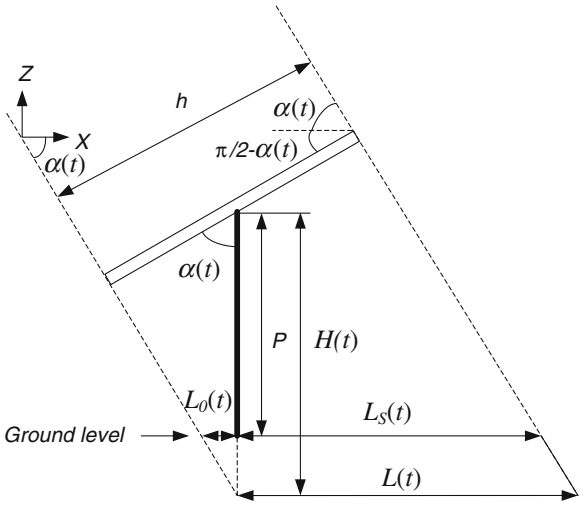

Fig. 6 Dimension of a dual-axis tracker at X–Z plane

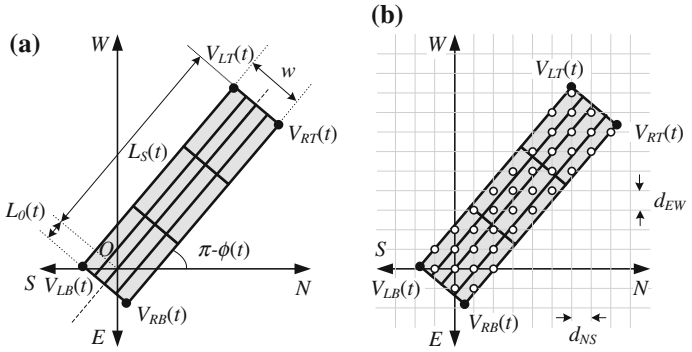

Fig. 7 Shadow by a dual-axis tracker with a 3-by-4 module array. **a** Shadow area on the ground. **b** Shadow matrix with grid

where w is the width of the module array; and $\phi(t)$ the θ as shown in Fig. 7a. When defining $V_{\mathrm{LB}}(t) = (x_{\mathrm{LB}}(t), y_{\mathrm{LB}}(t))$, $V_{\mathrm{LT}}(t) = (x_{\mathrm{LT}}(t), y_{\mathrm{LT}}(t))$, $V_{\mathrm{RB}}(t) = (x_{\mathrm{RB}}(t), y_{\mathrm{RB}}(t))$, and $V_{\mathrm{RT}}(t) = (x_{\mathrm{RT}}(t), y_{\mathrm{RT}}(t))$, four vertices of the (m, n) module in the M-by-N module array on a single tracker can be defined as

$$\begin{aligned}
V_{\mathrm{LB}}^{mn}(t) &= (x_{\mathrm{LB}}(t) + (m-1)(x_{\mathrm{LT}}(t) - x_{\mathrm{LB}}(t))/M + (n-1)(x_{\mathrm{RB}}(t) - x_{\mathrm{LB}}(t))/N, \\
&\qquad y_{\mathrm{LB}}(t) + (m-1)(y_{\mathrm{LT}}(t) - y_{\mathrm{LB}}(t))/M + (n-1)(y_{\mathrm{RB}}(t) - y_{\mathrm{LB}}(t))/N) \\
V_{\mathrm{LT}}^{mn}(t) &= \left(x_{\mathrm{LB}}^{mn}(t) + (x_{\mathrm{LT}}(t) - x_{\mathrm{LB}}(t))/M, y_{\mathrm{LB}}^{mn}(t) + (y_{\mathrm{LT}}(t) - y_{\mathrm{LB}}(t))/M\right) \\
V_{\mathrm{RB}}^{mn}(t) &= \left(x_{\mathrm{LB}}^{mn}(t) + (x_{\mathrm{RB}}(t) - x_{\mathrm{LB}}(t))/N, y_{\mathrm{LB}}^{mn}(t) + (y_{\mathrm{RB}}(t) - y_{\mathrm{LB}}(t))/N\right) \\
V_{\mathrm{RT}}^{mn}(t) &= \left(x_{\mathrm{RB}}^{mn}(t) + (x_{\mathrm{LT}}(t) - x_{\mathrm{LB}}(t))/M, y_{\mathrm{RB}}^{mn}(t) + (y_{\mathrm{LT}}(t) - y_{\mathrm{LB}}(t))/M\right)
\end{aligned} \tag{16}$$

Instead of calculating the shaded area for each tracker one by one, the shaded area can be efficiently obtained by using shadow- and Tracker-array matrixes. When letting a shadow matrix of the module array in the tracker be SM(t) with the solar north–south and the east–west grid as shown in Fig. 7b, each grid in the shaded area is assigned to a value of 1. With the same grid space, the (u, v) element of a Tracker-array matrix TA can be assigned to a value of 1 where a tracker is located at (u, v). Then the shadow matrix for the tracker array, SMA(t, u, v), can be calculated by a convolution as

$$\mathrm{SMA}(t, u, v) = \mathrm{TA}(u, v) \otimes \mathrm{SM}(t) \tag{17}$$

$$\mathrm{SMA}(t, u, v) = \sum_{p} \sum_{q} \mathrm{TA}(p, q)\mathrm{SM}(t, u - p, v - q) \tag{18}$$

where the installation site is sized by L_{EW}-by-L_{NS}; and $p = L_{EW}/d_{EW}$; and $q = L_{NS}/d_{NS}$. Then the shadow matrix for the all tracker arrays can be simplified as

$$\mathrm{SMA}(t) = \sum_{i=1}^{n_{EW}} \sum_{j=1}^{n_{NS}} \mathrm{SMA}(t, u_i, v_j) \tag{19}$$

where n_{EW} and n_{NS} are the number of tracker arrays in east–west and in north–south directions. From the shadow matrix, we can calculate the hours of shading for each grid points, $H_S(t_1, t_2)$, which describes how long each point is shaded by the tracker array for the given time from t_1 to t_2. Since the shadow matrix is discrete, we need to add time interval Δt, which leads to

$$H_S(t_1, t_2) = \Delta t \sum_{t=t_1}^{t_2} \mathrm{SMA}(t) \tag{20}$$

Figure 8a shows hours of shading by a single dual-axis tracker. The area beneath the module is most likely to be shaded, and the hours of shading are shaped like a butterfly. To identify how much a certain module in the tracker array is shaded at a given time t, SMA(t) in Eq. (19) can be rewritten as

$$\mathrm{SMA}(t) = \sum_{i=1}^{n_T} \sum_{j=1}^{n_S} \sum_{k=1}^{n_M} \mathrm{SMA}_{ijk}(t) \tag{21}$$

where n_T, n_S, and n_M are the number of trackers in the tracker array, strings in a tracker, and modules in a string, respectively. Defining $A_{ijk}(t)$ to be the shaded area on the ground by the kth module in the jth string on the ith tracker, the bar on it to be the self-shaded area on the module as shown in Fig. 8b, and the function $\sim$ to be

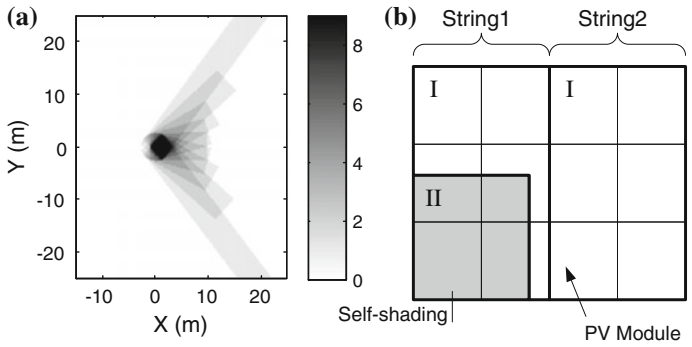

Fig. 8 **a** Hours of shading by a dual-axis tracker on January 1. **b** Example of self-shading in a 3-by-4 module array with two strings

the saturation function that makes each element be 1 if >1, then the fractions of self-shading on the module at a given time t can be obtained as

$$\begin{aligned} \mathrm{FS}_{ijk}(t) &= \overline{A_{ijk}(t)} \Big/ A_{ijk}(t) \\ &= \sum \sim \left[\mathrm{SMA}_{ijk}(t) - \sim \mathrm{SMA}_{ijk}(t)\right] \Big/ \sum \sim \mathrm{SMA}_{ijk}(t) \end{aligned} \tag{22}$$

5 Mismatch Between HCPV Modules

A PV module harvests its maximum energy when the voltage and the current are at its maximum power point $P_{\mathrm{MP}} = V_{\mathrm{MP}} \times I_{\mathrm{MP}}$. When a PV cell is shaded in a HCPV system, a bypass diode turns on and lets the string current flow with the reverse voltage across the cell. Deviations from the rated power of the individual cell or module can be caused by spectral mismatch, misalignment of optics, dirt, voltage drop on the cable, and so on. In [12], the effect of mismatch is analyzed using some worst-case scenarios. However, more generalizations is needed in planning utility-scale HCPV systems.

5.1 Power Losses Within a Module

Figure 9 shows current–voltage (I–V) and power–voltage (P–V) characteristics of a CPV module with two different tolerance values [13]. It is assumed that each parameter is normally distributed with 5 and 10 % SDs with their mean values. Each I–V curve has current steps that originated from a bypass diode connected to each cell. As tolerance increases, the voltage at the maximum power point also increases because of a decrease in the voltage drop across the internal series resistances. However, mismatches in current among cells increases accordingly and

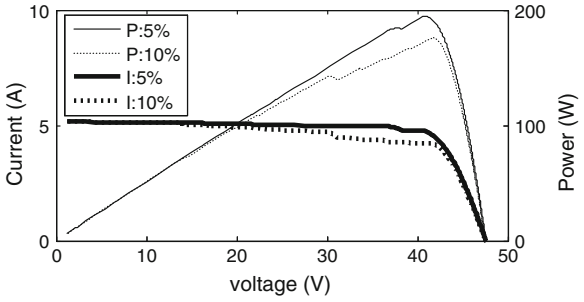

Fig. 9 I–V and P–V characteristics for a module with 5 and 10 % power tolerances

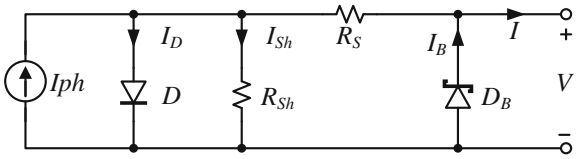

Fig. 10 Simple modeling of a PV cell

thus result in greater power loss. The mismatch losses increase from 0.9 to 6.2 % as tolerance increases from 5 to 10 %.

In HCPV system using multijunction PV cells, the high concentration of sunlight produces enough carriers to saturate the energy level of defects [14]. When the subcell generation–recombination current is neglected, a CPV cell with a bypass diode is modeled a shown in Fig. 10. The cell current I is given by

$$I = I_{\mathrm{Ph}} - I_{\mathrm{D}} - I_{\mathrm{Sh}} + I_{\mathrm{B}} \tag{23}$$

where I_{Ph}, I_{D}, I_{Sh}, and I_{B} are the PV currents that depend on irradiance and temperature, the internal diode current, the shunt current, and the bypass diode current, respectively. To understand the contribution of power losses, we instead consider five essential parameters including I_{Ph}, the diode saturation current I_{S}, the diode ideality factor n, the series resistance R_{S}, and the shunt resistance R_{Sh}. The simulation results based on these five parameters in terms of different tolerance given in Fig. 11 shows that power loss by mismatch is influenced by the order of $I_{\mathrm{Ph}} > n > R_{\mathrm{S}} \approx R_{\mathrm{Sh}} > I_{\mathrm{S}}$. Mismatch effects in the PV current are greater than others by more than several orders of magnitude regardless of the tolerance values.

5.2 Power Losses by Misalignments

Because the most dominant factor that causes power loss in HCPV systems is the mismatch in the PV current, HCPV system with a very narrow acceptance angle require highly accurate alignment control at the time of installation. Intramodule alignment can be accurately controlled in the factory. However, maintaining high

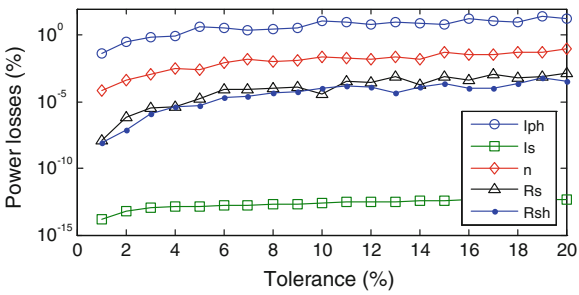

Fig. 11 Power losses in a CPV module by mismatches in various parameters

Fig. 12 *Bottom-right* view of misaligned HCPV modules

quality control during the time of installation is very difficult as can be seen from Fig. 12 [13]. Figure 13 shows a SolFocus prototype concentrator and its simulated optical efficiency $E(\theta_{C,i})$ according to the incident angle θ_C of the ith concentrator, which leads to the photocurrent of the ith cell as

$$I_{Ph,i} = I_{Ph0} \times E(\theta_{C,i}) \tag{24}$$

To account for module-to-module misalignments Eq. (24) can be redefined as

$$I_{Ph,i} = I_{Ph0} \times E(\theta_{C,i} + \theta_{M,j}) \tag{25}$$

where $\theta_{M,j}$ represents the angular misalignment of the jth module. Figure 14 shows the simulation results for power losses in 12 HCPV modules composed of 16 concentrators and all connected in series where σ_M is the SD of module-to-module alignment. Although the SD of $\theta_{C,j}$ is only $\sigma_C = 0.2°$, the module misalignment can easily be a dominant component by which to determine the power loss. By using an

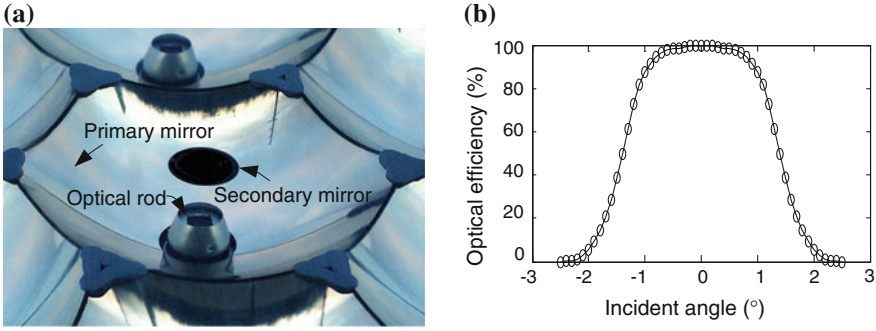

Fig. 13 SolFocus prototype HCPV concentrator. **a** Components. **b** Optical efficiency of the concentrator according to the incident angle

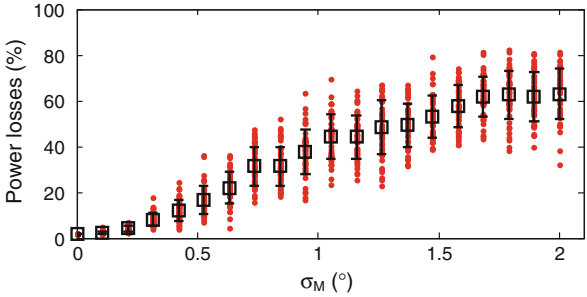

Fig. 14 Power losses by misalignment between modules (σ_C = 0.2°)

I–V curve as shown in Fig. 9, $V_{MP,ijk}$ and $I_{MP,ijk}$ can be obtained in term of voltage and current deviations, $\varepsilon_{V,ijk}$ and $\varepsilon_{I,ijk}$, as

$$V_{MP,ijk} = V_{MP}(1 + \varepsilon_{V,ijk}) \tag{26}$$

$$I_{MP,ijk} = I_{MP}(1 + \varepsilon_{I,ijk}) \tag{27}$$

6 Power-Optimization Strategies

As depicted in Fig. 15, various power-optimization strategies can be realized for HCPV systems [5, 13, 15]. Currently, centralized and string PV systems are mostly popular for utility-scale applications. However, considering mismatch and partial-shading losses, other types of distributed systems can be good candidates as

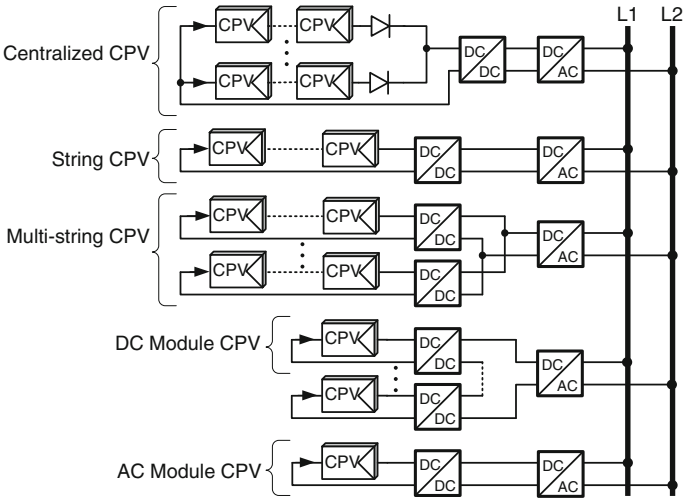

Fig. 15 Various power-optimization strategies of grid-tied HCPV systems

technology develops. Thus, quantifying the efficiencies of various strategies and choosing the optimum system are critical in lowering LCOE. In this section, various power-optimization strategies are investigated.

6.1 Centralized CPV System

Multiple string are connected in parallel followed by a single maximum power point tracker (MPPT) and an inverter, which makes each string voltage set the same. Let a CPV module have n_{BD} bypass diodes, and Eq. (22) be quantized by n_{BD} to consider mismatch and partial shading, then the DC power $P_{\mathrm{MP}}(t)$ based on each string can be obtained as

$$\mathrm{FS}_{ijk}(t) = \left\lceil n_{\mathrm{BD}}\mathrm{FS}_{ijk}(t)\right\rceil / n_{\mathrm{BD}} \tag{28}$$

$$V_{\mathrm{MP},ij}(t) = V_{\mathrm{MP}}\sum_{k=1}^{n_{\mathrm{M}}}\left[(1+\varepsilon_{\mathrm{V},ijk})(1-\mathrm{FS}_{ijk}(t)) - n_{\mathrm{BD}}V_{\mathrm{BD}}\mathrm{FS}_{ijk}(t)\right] \tag{29}$$

$$I_{\mathrm{MP},ij}(t) = \left\{\min(I_{\mathrm{MP},ijk}(t))\middle| k \in N, k \le n_{\mathrm{M}},\ \ \forall k : I_{\mathrm{MP},ijk}(t) \ge 0\right\} \tag{30}$$

$$P_{\mathrm{MP}}(t) = \left\{\sum_{i=1}^{n_{\mathrm{T}}}\max(V_{\mathrm{MP},ij}(t)\cdot\sum_{j=1}^{n_{\mathrm{S}}}I_{\mathrm{MP},ij}(t))\middle|\ j \in N, j \le n_{\mathrm{S}}\right\} \tag{31}$$

where $\mathrm{FS}_{ijk}(t)$ stands for the quantized shaded area using ceiling function to calculate the number of bypass diodes needed to be turned on. $V_{\mathrm{MP},ij}(t)$ and $I_{\mathrm{MP},ij}(t)$ are the maximum power point voltage and current of the jth string located in the ith tracker. Note that the efficiency of each DC/DC converter is reflected to the MPP voltage and current. The string current is assumed to be linearly proportional to the direct normal incident radiation I_{D} in Eq. (10) in terms of time.

6.2 String CPV System

Each string is connected to its own DC/DC converter and inverter for an individual MPPT, which makes each string independent of each other. A string CPV system offers a high DC string voltage range. Equation (28) through Eq. (31) are unchanged, and the DC power $P_{\mathrm{MP}}(t)$ based for each string can be obtained as

$$P_{\mathrm{MP}}(t) = \sum_{i=1}^{n_{\mathrm{T}}}\sum_{j=1}^{n_{\mathrm{S}}}V_{\mathrm{MP},ij}(t)\cdot I_{\mathrm{MP},ij}(t) \tag{32}$$

6.3 Multistring CPV System

The advantage of string CPV system is maximizing the string power independently. However, each string requires its own inverter, which requires additional cost. A multistring PV system takes advantage of having a central inverter per each tracker and optimizing power of each string independently. The basic condition is that each string voltage after DC/DC converters is uniform within a tracker. The DC power $P_{\mathrm{MP}}(t)$ based for multistring PV system can be obtained as

$$P_{\mathrm{MP}}(t) = \left\{ \sum_{i=1}^{n_{\mathrm{T}}} \sum_{j=1}^{n_{\mathrm{S}}} V_{\mathrm{MP},ij}(t) \cdot I_{\mathrm{MP},ij}(t) \middle| \; j_1 \neq j_2, \forall i : V_{\mathrm{MP},ij_1}(t) = V_{\mathrm{MP},ij_2}(t) \right\} \quad (33)$$

6.4 DC Module CPV System

In a DC module CPV system, each CPV module is connected to its own DC/DC converter that is in series with other DC/DC converters followed by an inverter. The main advantage of this scheme is maximizing energy harvest in each CPV module. The output voltage of each DC/DC converter is independently controlled, but the string current is uniform within a tracker. The DC power $P_{\mathrm{MP}}(t)$ based for a DC module PV system can be obtained as

$$V_{\mathrm{MP},ijk}(t) = V_{\mathrm{MP}}\left[(1 + \varepsilon_{\mathrm{V},ijk})(1 - \mathrm{FS}_{ijk}(t)) - n_{\mathrm{BD}} V_{\mathrm{BD}} \mathrm{FS}_{ijk}(t)\right] \quad (34)$$

$$I_{\mathrm{MP},ij}(t) = \left\{ I_{\mathrm{MP},ijk}(t) \middle| \; k_1 \neq k_2, \forall i,j : I_{\mathrm{MP},ijk_1}(t) = I_{\mathrm{MP},ijk_2}(t) \right\} \quad (35)$$

$$P_{\mathrm{MP}}(t) = \sum_{i=1}^{n_{\mathrm{T}}} \sum_{j=1}^{n_{\mathrm{S}}} \sum_{k=1}^{n_{\mathrm{M}}} V_{\mathrm{MP},ijk}(t) \cdot I_{\mathrm{MP},ij}(t) \quad (36)$$

6.5 AC Module CPV System (Microinverter CPV System)

Unlike other configurations, an AC module CPV system makes each CPV module completely independent from another one, which enhances power generation under self-shading and mismatch conditions. However, increased components may reduce the rated power under normal operation, and the higher cost for making electronics is a big hurdle for it to be applied for utility-scale CPV systems. $V_{\mathrm{MP},ijk}(t)$ is

identical to Eq. (34). The module current $I_{\mathrm{MP},ijk}(t)$ and the DC power $P_{\mathrm{MP}}(t)$ based for an AC module PV system can be obtained as

$$P_{\mathrm{MP}}(t) = \sum_{i=1}^{n_{\mathrm{T}}} \sum_{j=1}^{n_{\mathrm{S}}} \sum_{k=1}^{n_{\mathrm{M}}} V_{\mathrm{MP},ijk}(t) \cdot I_{\mathrm{MP},ijk}(t) \tag{37}$$

6.6 Centralized CPV System Without an MPPT

For the initial investment in a centralized CPV system to be lowered, which may not lead to lower LCOE, MPPT capability can be omitted and strings connected in parallel followed by a central inverter. In this case, the DC output voltage of a string is forced to a fixed ratio of its open-circuit voltage V_{OC} (e.g., 87 %). Because the partial-shading and mismatch losses are significant, this configuration is not recommended for utility-scale CPV systems. Basic equations for this configurations to calculate the total power harvested are as follows

$$V_{ij}(t) = 0.87 \cdot V_{\mathrm{OC},ij} \tag{38}$$

$$I_{ij}(t) = \left\{ I_{ijk}(t) \middle| \; k_1 \neq k_2, \; \forall i,j : \; I_{ijk_1}(t) = I_{ijk_2}(t) \right\} \tag{39}$$

$$P(t) = \sum_{i=1}^{n_{\mathrm{T}}} \sum_{j=1}^{n_{\mathrm{S}}} V_{ij}(t) \cdot I_{ij}(t) \tag{40}$$

7 Partial Shading Loss in Power-Optimization Schemes

Figure 16 illustrates the partial-shading effect in various power-optimization schemes. The 3-by-4 CPV modules on a dual-axis tracker are simulated for two different scenarios, in which the shades move (1) from bottom to top and (2) from left to right. For both cases, the power harvested by CPV modules within a single tracker is strong function of the amount and the shape of shading. The more the shading, in general, the less is the power harvested [16–18]. Distributed CPV systems using DC and/or AC modules are superior to others operating under these shading conditions, but the increased cost for electronics may cause increases in LCOE. For fair comparison, further careful analysis regarding the cost of electronics must be performed, which is out of scope for this section.

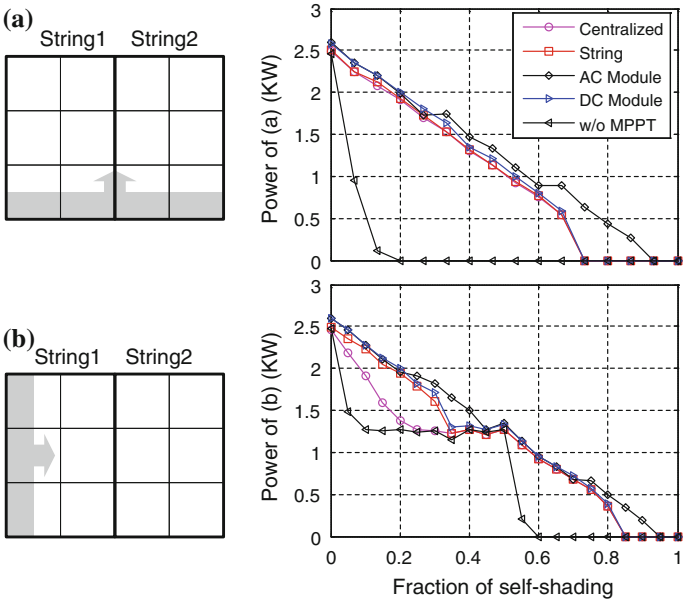

Fig. 16 Various power-optimization strategies of grid-tied HCPV systems

8 Tracker Array Model

The estimation of the total power harvested by a system requires accurate analysis of the geometrical configuration of both a tracker array and each module, especially for analyzing self-shading losses. Thus, all of the system parameters are extracted from the SolFocus prototype HCPV system in Fig. 17. Because most HCPV systems are built with a tracker array, GCR and CF in Eqs. (1) and (2), respectively,

Fig. 17 SolFocus prototype HCPV system used for extracting tracker and module parameters

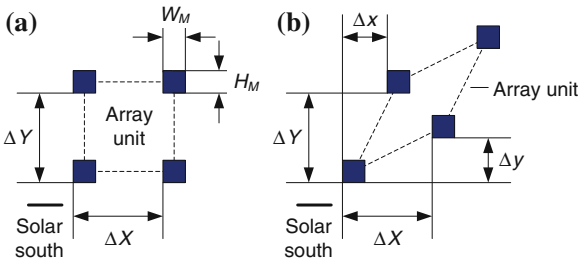

Fig. 18 Two types of tracker array units. **a** Rectangular array. **b** Quadrangular array

depend strongly on these geometries and can be redefined with an array unit as shown in Fig. 18.

$$\mathrm{GCR} = \sum A_{\mathrm{module}}/A_{\mathrm{land}} = W_{\mathrm{M}}H_{\mathrm{M}}/(\Delta X \Delta Y) \tag{41}$$

$$\mathrm{CF} = \frac{\sum_1^{365}\sum_1^{24} P(d,t)}{365 \cdot 24 \cdot P_{\max}} \tag{42}$$

where W_{M} and H_{M} are the width and the height of modules in a tracker, respectively, and $P(d, t)$ calculates total power harvested throughout a year on an hourly basis. Figure 19 shows shading by a 3-by-3 tracker array, located at the previously mentioned site, on January 1 at 8 AM. The darker color represents the overlapped shading area by multiple trackers. The more the space in between trackers, the less the self-shading happens.

When calculating the shadow matrix for the *m*-by-*n* tracker array as defined in Eqs. (19) and (21), the computational time is a linear function of the number of trackers. Especially for utility-scale simulations to optimize land use, this method might be too time-consuming. The algorithm in [7] makes the computation time

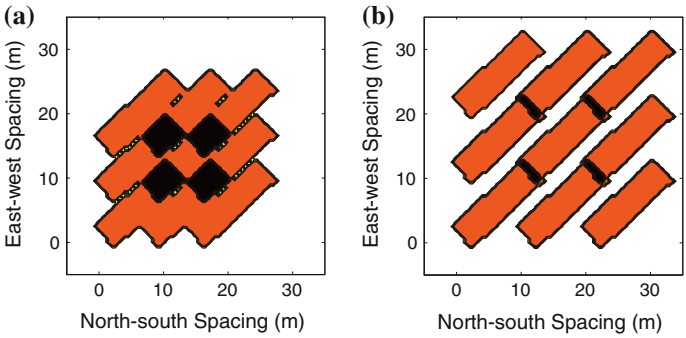

Fig. 19 Top view of shading by a 3-by-3 tracker array on January 1 at 8 AM **a** with 7-m spacing and **b** with 10-m spacing

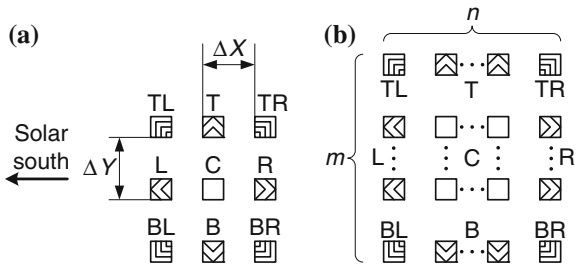

Fig. 20 Top view of a tracker array with CPV modules flat to the ground. **a** 3-by-3 tracker array. **b** *m*-by-*n* tracker array

independent of the scale of an HCPV system. Letting SMA(t) be a shadow matrix of a 3-by-3 tracker array at time t, SMA(t) can be separated into nine sections: (1) top left (TL), top, top right (TR), left, center, right, bottom left (BL), bottom, and bottom right (BR) as depicted in Fig. 20a. For calculating SMA(t) for the *m*-by-*n* tracker array, the array can also be divided into nine sections: $1 \times$ TL, $(n-2) \times$ T, $1 \times$ TR, $(m-2) \times$ L, $(m-2) \times (n-2) \times$ C, $(m-2) \times$ R, $1 \times$ BL, $(n-2) \times$ B, and $1 \times$ BR. Note that the most of trackers in *m*-by-*n* tracker array will be shaded, as with the center tracker in 3-by-3 tracker array, as the number of trackers increases.

9 Simulation Results

For comparison, we will consider two different simulations: simulation I for maximizing CF according to given GCR and simulation II for minimizing the cost function in Eq. (5) by varying the east–west and the north–south spacing. The procedure for each simulation I is as follows:

- Simulation I
  1. Gather monthly averaged DNI data for the site (only DNI is required for HCPV systems).
  2. Calculate hourly DNI from the monthly averaged DNI data.
  3. Find the *m*-by-*n* tracker array with a given GCR that maximizes CF by using the shadow matrix.
  4. Calculate the optimal CF according to GCR.
  5. Repeat steps 3 and 4 for various power-optimization schemes.

Figure 21 shows DC energy harvested by an *m*-by-*m* tracker array based on the simulation I where ΔX, ΔY, Δx, and Δy are set to 10, 10, 0, and 0 m, respectively. The modeling can be applied to any type of tracker and module array. It can be seen that the lager tracker array gives more self-shading energy loss, especially in the

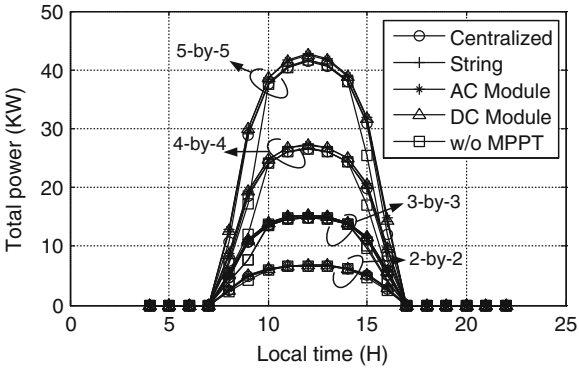

Fig. 21 DC energy harvested by an *m*-by-*m* tracker array on January 1 where GCR = 0.2 and 3-by-4 modules are on each tracker

morning and the evening. DC module–based and AC module–based CPV systems alleviate mismatch losses among CPV modules; thus, they harvest more energy than other types of power-optimization scheme even at solar noon without self-shading. In a centralized PV system, a shaded string may affect the performance of the unshaded strings resulting in equal or lower power harvest than other types.

Each power-optimization scheme for the 4-by-4 module array is compared in Fig. 22. Orientation of the tracker array is set to the mean value of solar noon to minimize the maximum shadow length by each tracker. For fast simulation, hourly DNI on the first day of each month is considered. Tracker array and sampling days can be larger at the expense of longer computational time. The CF-versus-GCR plot shows the optimum spacing of the tracker array. As GCR increases, the optimum CF decreases due to aggravated self-shading losses. However, in Fig. 22, the values of GCR and CF for minimizing LCOE cannot be obtained. Thus, we needs to obtain the cost function as follows:

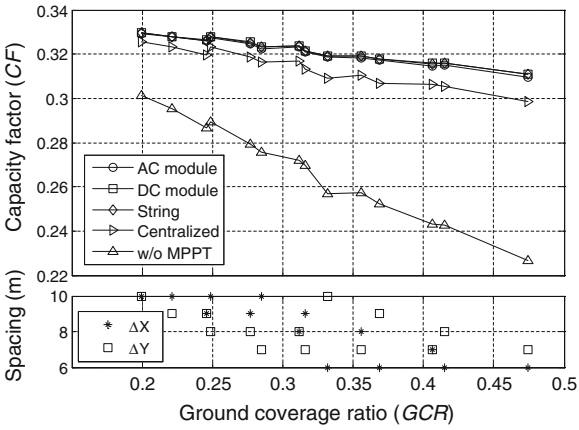

Fig. 22 Capacity factor for various ground coverage ratios of a 4-by-4 tracker array. Optimum spacing among dual-axis trackers is given for each point

- Simulation II

1. Perform steps 1 and 2 from the simulation I.
2. Obtain the value of k in the cost function.
3. Find the 3-by-3 shadow matrix and calculate the overall power and the cost function.
4. Based on the step 3, calculate the overall power that minimizes the cost function of the m-by-n tracker.
5. Repeat steps 3 and 4 for various power-optimization schemes.

Figure 23 depicts hours of shading by a 3-by-3 tracker array. The simulation only includes time with $\alpha < 0$. As with simulation I, the first day of each month is sampled for reducing the computational time. The darker the color at the particular points, the more the hours of shading occur. It can be seen that more shading occurs in the east–west direction than that in the north–south direction, which indicates that greater spacing is required for the east–west direction.

The most narrow tracker spacing that minimizes the cost function according to the value of k is shown in Fig. 24 based on DNI from NASA. To investigate the dependency of tracker size, both 3-by-3 and m-by-n arrays (where $m = n = 20$) are simulated and compared. Trackers located on the boundary of the 3-by-3 array are affected less by shading than the tracker in the center. However, the portion of trackers located on the boundary of the m-by-n array is smaller than that of the 3-by-3 array, resulting in more self-shading losses. Therefore, larger spacing is required for m-by-n array. The range of spacing is limited to $7 \leq \Delta X \leq 11$ and $7 \leq \Delta Y \leq 12$ for reducing the run time. DNI data from TMY3 are applied to the same analysis as depicted in Fig. 25. The values of ΔX are equal or less than those from Fig. 24 mainly due to lower DNI in winter TMY3 data. The optimization is weighted more to performance in the summer. Finally, the run time to obtain data for Fig. 22 is linear to the number of trackers; however, the run time to obtain Figs. 24 and 25 takes 13 min with a 2.2-GHz dual-core processor regardless of the number of trackers.

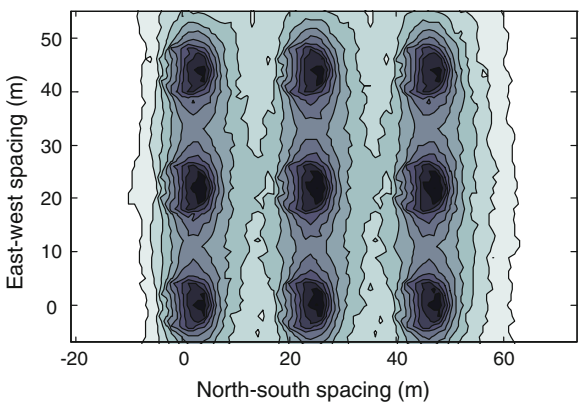

Fig. 23 Hours of shading by a 3-by-3 tracker array with both east–west and north–south spacing of 11 m

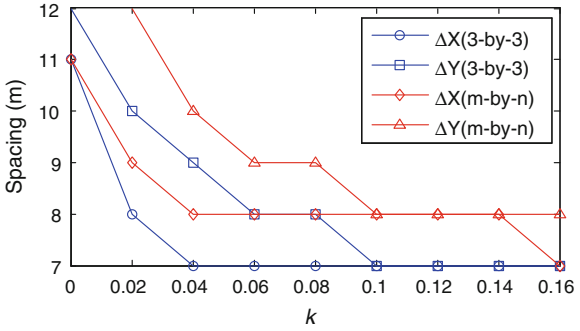

Fig. 24 Most narrow tracker spacing that minimizes the cost function with DNI data from NASA

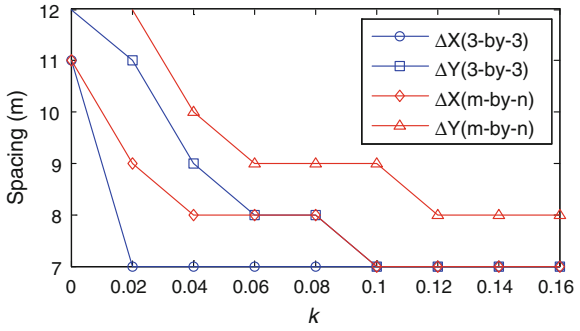

Fig. 25 Most narrow tracker spacing that minimizes the cost function with DNI data from TMY3

10 Conclusion

This chapter presents a comprehensive model of HCPV systems including location-dependent DNI, various configurations of tracker and module arrays, mismatch and misalignment, and power-optimizing schemes. This model can be widely used by the solar industry to estimate how much energy can be generated with given system parameters and to maximize energy harvest of the system. Moreover, the cost function that considers CF, GCR, and the relative cost of land minimizes the LCOE cost of energy by optimizing the space among dual-axis trackers. For fast simulation, the performance of a 3-by-3 tracker array is matched to an *m*-by-*n* tracker array resulting in a constant run time regardless of the number of trackers.

Acknowledgments This work was supported by the Human Resources Development program (Grant No. 20124030200120) of the Korea Institute of Energy Technology Evaluation and Planning grant funded by the Korea government Ministry of Trade, Industry and Energy. This research was also supported by Basic Science Research Program through the National Research Foundation of Korea (NRF) funded by the Ministry of Science, ICT and Future Planning (Grant No. NRF-2014R1A1A1003771).

References

1. Roy S (2006) optimal planning for utility generation by photovoltaic sources spread across multiple sites. IEEE Trans Energy Conv 21:181–186
2. Carrasco JM, Franquelo LG, Bialasiewicz JT, Galvan E, Guisado RCP, Prats MAM, Leon JI, Moreno-Alfonso N (2006) Power-electronic systems for the grid integration of renewable energy sources: A survey. IEEE Trans. Ind. Electron. 53:1002–1016
3. Campbell M, Blunden J, Smeloff E, Aschenbrenner P (2009) Minimizing utility-scale PV power plant LCOE through the use of high capacity factor configurations. In: Proceedings of photovoltaic specialists conference, June 2009, pp 421–426
4. Narvarte L, Lorenzo E (2008) Tracking and ground cover ratio. Prog Photovoltaics Res Appl 16(8):703–714
5. Kim YS, Kang SM, Winston R (2013) Modeling of a concentrating photovoltaic system for optimum land use. Prog Photovoltaics Res Appl 21(2):240–249
6. Panico D, Garvison P, Wenger H, Shugar D (1991) Backtracking: a novel strategy for tracking PV systems. In: Proceedings of photovoltaic specialists conference, Oct 1991, pp 668–673
7. Kim YS, Winston R (2011) Optimal spacing of dual-axis trackers for concentrating photovoltaic systems. In: 7th international conference on concentrating photovoltaic systems: CPV-7, Apr 2011, pp 370–373
8. Walraven R (1978) Calculating the position of the sun. Sol Energy 20:393–397
9. Duffie JA, Beckman WA (2013) Solar engineering of thermal process. Wiley, New York
10. Kasten F, Young AT (1989) Revised optical air mass tables and approximation formula. Appl Opt 28:4735–4738
11. Meinel AB (1976) Applied solar energy: an introduction. In: Addison-Wesley series in physics
12. Spertino F, Akilimali JS (2009) Are manufacturing mismatch and reverse currents key factors in large photovoltaic arrays? IEEE Trans Ind Electron 56:4520–4531
13. Kim YS, Kang SM, Winston R (2014) Tracking control of high concentration photovoltaic systems for minimizing power losses. Prog Photovoltaics Res Appl 22(9):1001–1009
14. Minuto A, Timò G, Groppelli P, Sturm M (2010) Concentrating photovoltaic multijunction (CPVM) module electrical layout optimisation by a new theoretical and experimental "mismatch" analysis including series resistance effects. In: Proceedings of photovoltaic specialists conference, June 2010, pp 3081–3086
15. Kim YS, Winston R (2014) Power conversion in concentrating photovoltaic systems: central, string, and micro-inverters. Prog Photovoltaics Res Appl 22(9):984–992
16. Patel H, Agarwal V (2008) Maximum power point tracking scheme for PV systems operating under partially shaded conditions. IEEE Trans Ind Electron 55:1689–1698
17. Gao L, Dougal RA, Liu S (2009) Parallel-connected solar PV system to address partial and rapidly fluctuating shadow conditions. IEEE Trans Ind Electron 56:1548–1556
18. Carannante G, Fraddanno C, Pagano M, Piegari L (2009) Experimental performance of MPPT algorithm for photovoltaic sources subject to inhomogeneous insolation. IEEE Trans Ind Electron 56:4374–4380